Cavity quantum electrodynamics with charge-controlled quantum dots coupled to a fiber Fabry–Perot cavity

Javier Miguel-Sánchez, Andreas Reinhard, Emre Togan, Thomas Volz, Atac Imamoglu, Benjamin Besga, Jakob Reichel, Jérôme Estève

PAPER • OPEN ACCESS

Cavity quantum electrodynamics with charge-controlled quantum dots coupled to a fiber Fabry–Perot cavity

To cite this article: Javier Miguel-Sánchez *et al* 2013 *New J. Phys.* **15** 045002

New Journal of Physics
The open access journal for physics

Cavity quantum electrodynamics with charge-controlled quantum dots coupled to a fiber Fabry–Perot cavity

Javier Miguel-Sánchez[1,3], Andreas Reinhard[1], Emre Togan[1], Thomas Volz[1], Atac Imamoglu[1], Benjamin Besga[2], Jakob Reichel[2] and Jérôme Estève[2]

[1] ETH Zürich, Institute for Quantum Electronics, Wolfgang-Pauli-Strasse 16, HPT G5, 8093 Zürich, Switzerland
[2] Laboratoire Kastler Brossel, ENS, UPMC-Paris 6, CNRS, 24 rue Lhomond, F-75005 Paris, France
E-mail: sanchez@phys.ethz.ch

New Journal of Physics **15** (2013) 045002 (18pp)
Received 19 November 2012
Published 4 April 2013
Online at http://www.njp.org/
doi:10.1088/1367-2630/15/4/045002

Abstract. We demonstrate non-perturbative coupling between a single self-assembled InGaAs quantum dot and an external fiber-mirror-based microcavity. Our results extend the previous realizations of tunable microcavities while ensuring spatial and spectral overlap between the cavity mode and the emitter by simultaneously allowing for deterministic charge control of the quantum dots. Using resonant spectroscopy, we show that the coupled quantum dot cavity system is at the onset of strong coupling, with a cooperativity parameter of $C \approx 2.0 \pm 1.3$. Our results constitute a milestone in the progress toward the realization of a high-efficiency solid-state spin–photon interface.

[3] Author to whom any correspondence should be addressed.

Contents

1. Introduction

The interaction between a quantum emitter and a single optical cavity mode, termed cavity quantum electrodynamics (QED), has allowed for a number of key experimental advances in quantum optics, including the observation of an enhancement of spontaneous emission [1], the demonstration of the photon blockade effect [2] and vacuum-induced transparency [3]. A key requirement for the observation of the heretofore-mentioned phenomena is a large cooperativity parameter ($C = 2g^2/\kappa\gamma$) [4], which is attained if the square of the coupling strength (g) between the emitter and the mode exceeds the product of the emitter (γ) and the mode (κ) energy decay rates. Minimizing the ratio of the cavity mode volume (V) to its quality factor (Q) allows maximizing of C, provided that the emitter is located at a maximum of the cavity electric field (spatial overlap) and that the resonance frequency of the emitter and the mode are identical to each other (spectral overlap).

The condition $C \gg 1$ has been achieved for a number of different emitters and cavity designs, ranging from single atoms coupled to Fabry–Perot cavities [2, 5] or on-chip micro-toroids [6] to super-conducting qubits in coplanar waveguide resonators working in the microwave domain [7]. A technologically very relevant all-solid-state cavity QED platform in the optical domain consists of quantum dots (QDs) coupled to nano-fabricated cavities [8–10]. However, for these integrated devices, to achieve spectral and spatial overlap has been a major challenge. Even though techniques that overcome these limitations using state-of-the-art nanotechnology methods have been demonstrated [11–13], a flexible cavity design where a large C can be achieved for every QD would greatly improve the prospects of novel solid-state cavity–QED experiments.

In this paper, we demonstrate that $C \approx 2.0 \pm 1.3$ by coupling the excitonic transitions of single self-assembled QDs to a hybrid cavity structure that consists of a GaAs/AlAs-based distributed Bragg reflector (DBR) mirror below the QD layer, and a curved fiber-end mirror approached from the top. Spectral and spatial overlap in this structure is achieved by

moving the sample with respect to the fixed top mirror. Previous attempts with QDs in similar hybrid structures realized C values well below 1 [14–16]. Besides the significantly enhanced cooperativity value in the present setup, the main novel feature is the fact that our QDs are embedded in a p–i–n structure: by separately contacting the p and n layers electrically and applying a gate voltage, we achieve full charge control of the QDs. This in turn opens up the path to perform cavity–QED experiments where optical transitions address given QD spin states. We thus demonstrate a fully tunable spin–cavity–QED system requiring a minimum of technological steps, together with fiber-coupled optical output, that can, in principle, satisfy the high collection efficiency requirement of quantum information processing protocols.

2. Cavity–quantum dot (QD) coupling

The dynamics of a two-level emitter, e.g. an excitonic QD transition, coupled to a single cavity mode is accurately described by the so-called Jaynes–Cummings model [17]. The Hamiltonian includes a coupling term between the cavity and the emitter, which is characterized by an angular frequency g, also called the coupling strength [18]:

$$g = \left(\frac{1}{4\pi\epsilon_0} \frac{\pi e^2 f}{m_0 V_m} \right)^{1/2}. \tag{1}$$

Here, f is the oscillator strength of the emitter transition, m_0 is the electron mass and V_m is the effective mode volume which is defined as

$$V_m = \frac{\int \epsilon_r(\mathbf{r}) \, |\mathbf{E}(\mathbf{r})|^2 \, \mathrm{d}^3 r}{\max |\mathbf{E}(\mathbf{r})|^2}, \tag{2}$$

$\epsilon_r(\mathbf{r})$ is the dielectric function, whereas $\mathbf{E}(\mathbf{r})$ denotes the intracavity electric field. This coupling is proportional to the scalar product of emitter dipole and the intra-cavity electric field generated by a single photon. Equation (1) gives the maximal value of the coupling parameter g assuming that the emitter is located at the maximum of the electric field and has the same polarization. A small cavity volume enhances the coupling. For a strong enough coupling, the transmission and reflection of the coupled system are significantly modified compared to the bare cavity at the condition that the emitter and the cavity can be brought to resonance [19, 20]. The effects of the cavity–emitter coupling can be quantified by the cooperativity C. In the large cooperativity limit, a significant portion of the emitted light ends in the cavity mode which can be efficiently extracted, making $C \geqslant 1$ a desirable operating range for many applications including quantum information processing. It is also well known that $C \geqslant 1$ is required for obtaining strong photon–photon interactions. Last but not least, the fidelity of cavity-mediated qubit–qubit interactions typically scales with C. To achieve $C \geqslant 1$ is challenging and generally requires careful engineering of the coupling. A common technique for increasing g is by reducing the cavity volume and positioning the QD at the cavity field maximum.

Usually, epitaxial QDs are randomly distributed on the wafer surface. Experiments have tried to achieve spatial matching by defining a nano-fabricated array of cavities on top of the randomly distributed QDs. Even though strong coupling could be observed this way, the chance for close-to-optimal coupling is rather low. More sophisticated methods for relative alignment of the QD and the cavity mode have been reported in the literature. The first approach controls the position of the QDs on the wafer during growth by nucleation sites [12, 21, 22]. In the second

approach, the cavity is written around single pre-selected (randomly distributed) QDs that are precisely located on the wafer by SEM metrology [11, 23] or optical spectroscopy [13, 24, 25].

Even though these approaches enable excellent spatial overlap, the resonance frequencies of the cavity and the QD are generally different, which implies the need for post-processing tuning mechanisms to bring the system into resonance. Besides the irreversible fine-tuning by digital etching [26], an *in situ* reversible tuning mechanism for photonic-crystal cavities by means of adsorbing/desorbing gas molecules was demonstrated [27] and is now widely used in many laboratories. The hybrid cavity–QED approach we detail here stands in stark contrast to these earlier approaches, since it allows for a much more straightforward spatial and spectral alignment with any of the QDs on a given device.

3. Experimental setup

Our semi-integrated hybrid cavity system consists of a sample-based DBR mirror below an active QD layer and a curved fiber-end mirror (figure 1(a)) which is approached from the top. The details of the fabrication of the fiber can be found in [28]. The sample is mounted on a stack of piezoelectric nanopositioners for precise positioning in all three spatial dimensions. The fiber in turn is fixed above the sample surface as illustrated in figure 1(b). For performing photoluminescence spectroscopy, an intensity-stabilized pulsed Ti : sapphire laser at 785 nm is used. The system is excited through the DBR-coated fiber mirror close to a reflectivity minimum of the mirror. The PL is collected through the same fiber and sent to a high-resolution grating spectrometer with a nitrogen-cooled CCD camera for recording the spectrum. For resonant spectroscopy, a mode-hop free intensity-stabilized diode laser, tunable from 890 to 910 nm, is sent through the fiber, and the transmitted light is collected on a silicon detector mounted at the bottom of the sample (henceforth referred to as a transmission detector). The transmission signal is expected to be orders of magnitude larger than the resonant reflection signal due to the considerably higher reflectivity of the top fiber mirror (transmission and losses for this mirror are 55 and 28 ppm, respectively). The transmission signal is directly amplified by a high-gain low-noise amplifier. The sample and fiber are part of a home-built cage system that is inserted into a buffer-gas-filled dipstick, which in turn sits in a liquid He dewar and is kept cold at 4 K.

4. Fiber mirror cavity

4.1. Cavity modes

To a good approximation, the cavity can be considered as a planar-concave Fabry–Perot cavity whose properties are determined by the radius of curvature R of the concave mirror at the tip of the fiber and by the length L of the gap between the fiber and the substrate. A given cavity mode is characterized by its polarization and by three integers q and m, n, which label the longitudinal and the transverse mode structure, respectively. For a curved mirror with rotational symmetry, one would expect the transverse modes with equal values of $m+n$ to be degenerate. As figure 2(a) illustrates, in our system, modes with identical values of $m+n$ are non-degenerate, because of the slight ellipticity of the fiber mirror, which is induced by imperfections of the fabrication. In addition, all the modes exhibit a polarization splitting as demonstrated for the TEM_{00} mode in the inset of figure 2(a). In the remainder of this paper, we label the two orthogonally polarized modes as TEM_{00}^{A} and TEM_{00}^{B}.

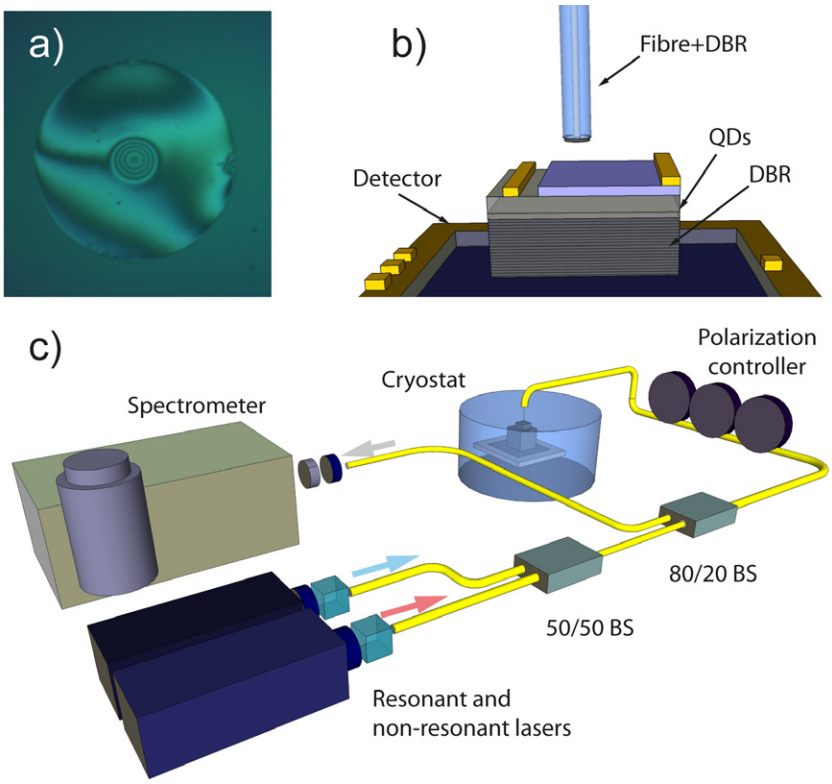

Figure 1. Setup of the semi-integrated QD–cavity system. (a) The top mirror of the Fabry–Perot-type cavity consists of a highly reflective dielectric DBR mirror at the tip of a standard single-mode optical fiber. The central Gaussian recess leads to a denser set of interference rings in the profilometer picture shown. (b) The planar bottom DBR mirror is made up of 28 GaAs/AlAs layers with the active QD layer on top. The relative distance between the fiber end and the sample controls the cavity length and thereby the cavity resonance frequency. (c) Experimental setup: off-resonant and near-resonant lasers are used to excite and probe the QD–cavity system by photoluminescence and transmission spectroscopy, respectively. Luminescence is collected through the same fiber that is used to excite the sample in the liquid-helium bath cryostat and analyzed on a grating spectrometer with an integrated CCD chip. Fiber paddles control the polarization of the resonant laser light before it enters the cryostat.

These effects are summarized by the following equation which gives the resonance frequency of a mode:

$$\nu_{qmn}^{A,B} = \frac{c}{4\pi L}\left[2\pi q + (2m+1)\arccos\sqrt{1-\frac{L}{R_x}} + (2n+1)\arccos\sqrt{1-\frac{L}{R_y}} + \phi(\nu_{qmn}^{A,B}) \pm \delta\right]. \quad (3)$$

The A and B symbols distinguish the two eigenpolarizations which correspond to two orthogonal linearly polarized modes. The associated phase $-(+)\delta$ for the A (B) mode is a consequence of the small birefringence present in both DBR mirrors and is of the order of 10 mrad. The two curvature radii R_x and R_y account for the ellipticity of the fiber mirror (the

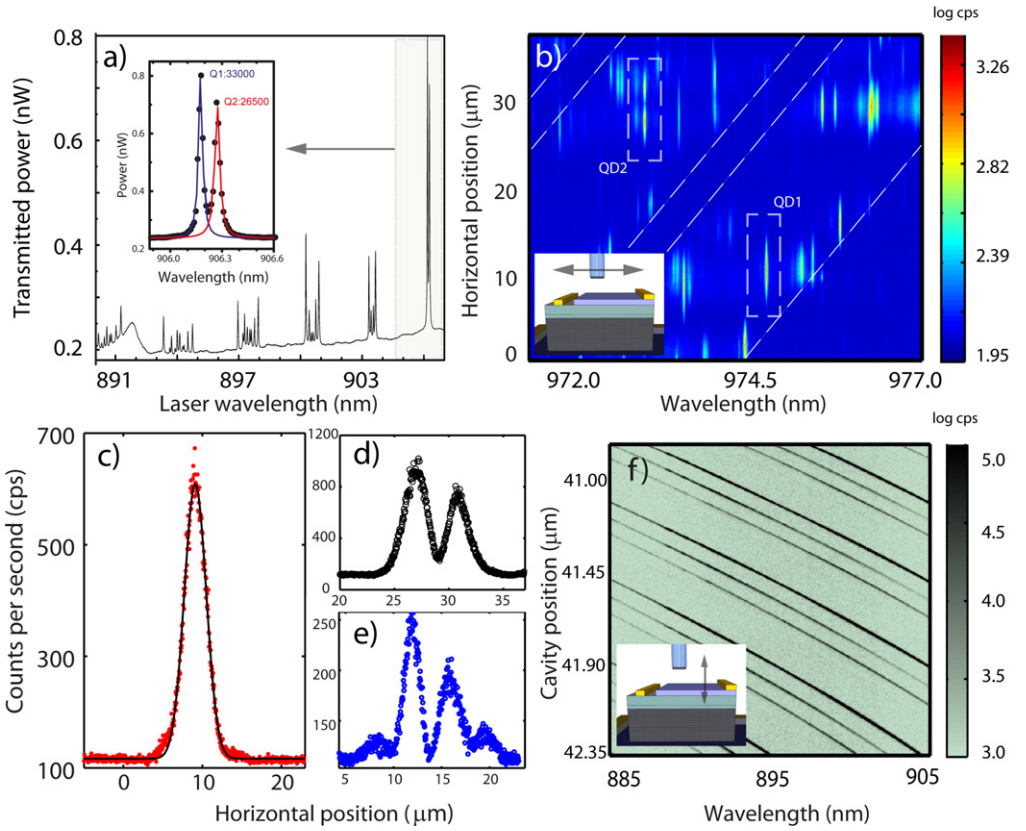

Figure 2. (a) Cavity transmission as a function of laser wavelength in the range between 890 and 907 nm. The different groups of cavity resonances correspond to different transverse modes with the same number of transverse excitations $n+m$. The resonance with the lowest energy is the fundamental TEM_{00} mode which is split into two linearly polarized modes, TEM_{00}^{A} and TEM_{00}^{B}. The splitting between these modes amounts to 144 μeV. (b) Transverse mode profiles: by scanning the sample in the transverse direction, the mode profiles of the different transverse cavity modes are mapped out by recording the luminescence from the system as a function of position. Due to a slight wedge in the sample, the data were recorded using a slow modulation technique in the z-direction to always ensure coupling of the QDs to the cavity mode. This leads to 'PL gaps' indicated by the tilted dashed white lines (see the appendix for details). (c) Gaussian fit (black) to the fundamental TEM_{00} mode (red) measured in (b), with a ω_0 of 2.7 μm. Panels (d) and (e) show higher-order transverse mode profiles (QD3 not shown in scan (b)). (f) Luminescence from the cavity modes as a function of cavity length, demonstrating the tunability of the cavity resonance frequency. Due to off-resonant cavity feeding, the cavity modes are visible over a wide range of wavelengths.

two values typically differ by a few per cent), and the phase $\phi(\nu)$ is the sum of the phases acquired through the reflection on each DBR. This phase varies slowly around the common central wavelength of the DBRs and can be considered as a constant to first approximation

($\phi \approx \pi$ for our sample), allowing direct determination of the mode frequency. In order to calculate resonance frequencies beyond this approximation, equation (3) must be solved with the frequency dependence of the phase included explicitly, which can be determined using numerical methods, such as the transfer matrix method.

We expect the transverse distribution of the electric field in one m, n mode to be given by the corresponding Hermite–Gauss function. This dependence can be observed by laterally scanning the fiber above the sample and monitoring the emitted fluorescence collected through the fiber on a spectrometer (see figure 2(b)). As the QD is much smaller in size compared to the wavelength of light, and the fiber only collects light in the cavity mode at the cavity resonance, scanning QDs in space while exciting with a non-resonant laser power above saturation gives a very accurate measurement of the cavity mode profile. Plotting the integrated fluorescence in a narrow frequency window against the lateral fiber position therefore gives a cut of the intensity profile of this mode assuming only one QD to be present in the narrow frequency window. Figures 2(c)–(e) show three profiles obtained from such measurements. As expected for the fundamental mode, the profile quite accurately fits to a Gaussian (figure 2(c)).

The tunability of the cavity is assessed in figure 2(f). By collecting PL while slowly decreasing the cavity length, we observe how we can access smoothly many free spectral ranges (FSRs) to couple the QDs to any cavity energy for many different lengths. Emission from cavity modes is observed in a wide range owing to the fact that this particular scan was performed in a sample region with a high QD density. The large variation of QD sizes is responsible for the broad band emission. Being able to choose the cavity length while working with the same QD also opens up the possibility to build cavities with very long lifetimes. For example, the value of the quality factor $Q \approx 30\,000$ reported in the inset of figure 2(a) can be significantly increased (we have been able to measure $Q > 60\,000$) if it is needed in a specific experiment. These values may be influenced by the absorption in the doped layers of the semiconductor structure.

4.2. Cavity mode volume

Considering a TEM_{00} mode, the effective mode volume is given by $\pi w_0^2 L_{\mathrm{eff}} \beta/4$, where w_0 is the mode waist on the substrate, $\beta = |\mathbf{E}_{\mathrm{vac}}|^2 / \max |\mathbf{E}(\mathbf{r})|^2$ is the ratio of the field maximum in the vacuum to the maximum in the whole cavity (for our sample $\beta = 0.98$) and L_{eff} is the effective length of the mode including the penetration depth of the cavity field into the DBRs, extracted from transfer matrix calculation [18, 29, 30]:

$$L_{\mathrm{eff}} = L_{\mathrm{DBR}}^{\mathrm{fiber}} + L_{\mathrm{geo}} + n_{\mathrm{GaAs}}^2 (L_c + L_{\mathrm{DBR}}^{\mathrm{semic}}) \tag{4}$$

with

$$L_{\mathrm{DBR}}^{\mathrm{fiber}} = \frac{1}{2} \frac{\lambda_0}{2(n_{\mathrm{Ta_2O_5}} - n_{\mathrm{SiO_2}})} \tag{5}$$

and

$$L_{\mathrm{DBR}}^{\mathrm{semic}} = \frac{1}{2} \frac{\lambda_0 n_{\mathrm{GaAs}} n_{\mathrm{AlAs}}}{2 n_{\mathrm{GaAs}}^2 (n_{\mathrm{GaAs}} - n_{\mathrm{AlAs}})}, \tag{6}$$

where L_{geo} is the distance between the fiber mirror end and the semiconductor surface. For our sample, we obtain $L_{\mathrm{eff}} = L_{\mathrm{geo}} + 7.6\,\mu\mathrm{m}$. The waist w_0 can be estimated from Gaussian optics to be

$$w_0 = [\lambda^2 L(R - L)/\pi^2)]^{1/4}. \tag{7}$$

In order to minimize the mode volume and thus maximize the cavity/emitter coupling, both L and R should be minimized. Using the CO_2 laser ablation technique, radii down to 10 μm have been reported. Here, we use a fiber mirror with a radius of curvature of the order of 75 μm [28]. The smallest L that can be achieved is often limited by geometrical aspects such as the depth of the mirror structure at the fiber tip (of the order of a few μm) and/or surface defects at the fiber tip. These are, however, not fundamental reasons, and cavities with lengths L of the order of a few wavelengths could, in principle, be fabricated. This sets the minimal waist ω_0 for this type of cavity to lie between 1 and 1.5 μm for a design wavelength close to 1 μm. In the following, we minimize L by moving the fiber down until it touches the substrate and we step back by a few hundred nanometers. From the coupling strength to the QD that we measured (see section 8), we can estimate the effective mode volume to be smaller than 150 λ_{air}^3 for our current setup ($\lambda_{\mathrm{air}} = 900$ nm).

5. The device: charge-controlled QDs

A schematic diagram of the sample is shown in figure 3(a). It was grown by molecular beam epitaxy (MBE) on a GaAs (100) substrate. The epitaxial structure growth starts with a 300 nm GaAs buffer, followed by 28 pairs of AlAs/GaAs that form the bottom mirror of the cavity, which sets the timescale for the photon lifetime in the cavity since it has lower reflectivity than the top fiber mirror. The reflectivity of the bottom mirror was measured over the relevant wavelength range at room temperature and is plotted in figure 2(c). The interference pattern below 860 nm is slightly smoothed out due to absorption by the GaAs layers as was also confirmed by a transfer matrix calculation.

A key feature of our system is the tunability of the exciton energy and the control of the QD charging state. This is achieved by a p–i–n structure on top of the AlAs/GaAs DBR. The n-layer consists of a 40 nm Si-doped GaAs layer with a carrier concentration of $\approx 1 \times 10^{18}$ cm^{-3}, while the top p-layer is a 35 nm wide GaAs layer doped with C atoms. The QDs are sandwiched between the two conductive layers and were grown without rotating the substrate to ensure a smooth gradient in QD density across the wafer. The QD layer is separated from the conductive n-layer through a 40 nm tunnel barrier of undoped GaAs. An additional AlGaAs blocking barrier was introduced between the QD and the p-doped region. In the experiments reported here, we used two different samples, with the QD emission wavelengths centered at 900 and 970 nm, respectively. The emission energy of the QDs was controlled by using the partially covered island method [31]. The overall thickness of all the layers on top of the DBR mirror amounts to λ/n, i.e. one optical wavelength. This ensures that the QD layer will be at an antinode of the cavity field along the growth direction. The p- and the n-layers result in an intrinsic electrical field that can be modulated by applying an additional external bias voltage. For contacting the sample, the processing procedure was as follows: in a small portion of the sample, the top $\approx$80 nm were removed by wet etching with $H_2SO_4 : H_2O_2 : H_2O$. In a second step, an Ohmic contact to the n-doped layer was formed by annealing some indium on the sample surface for 360 s at an oven temperature of around 350 °C. The highly doped p-layer was contacted using silver paint deposited on the sample surface. The I–V curve of the final device is displayed in figure 3(b). The deviations from the ideal diode curve arise from the very simple processing protocol and unavoidable imperfections in the sample due to microscopic structural defects. Due to the p–i–n structure of the device, the application of a bias voltage induces current flow of both electrons and holes which—through relaxation into the QDs and the wetting layer—leads to

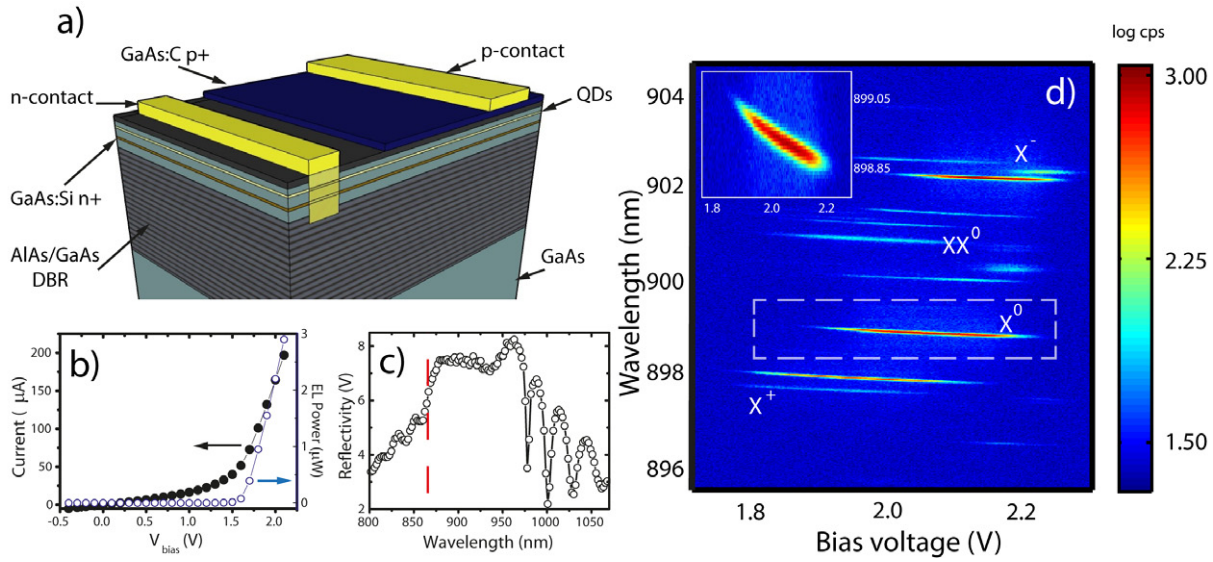

Figure 3. (a) Device structure. In order to control the charge of the QDs, an n-doped GaAs layer below, together with a p-doped GaAs layer above the actual QD layer, forms a p–i–n diode structure. An additional AlGaAs blocking barrier between the QD layer and the p-doped region prevents excessive current flow. (b) The *I*–*V* characteristic (black) for the p–i–n diode and electroluminescence signal (blue) as a function of the applied gate voltage at low temperature. (c) Measured reflectivity of the semiconductor DBR mirror between 800 and 1050 nm. The vertical dashed red line indicates the GaAs bandgap energy. A minimum in reflectivity around 940 nm arises from a systematic measurement error. (d) QD charging plateaus. PL signal (logarithmic scale) as a function of gate voltage and wavelength. The different voltage regions corresponding to the different charging plateaus of the same QD are clearly visible. The inset shows a blow-up of the X^0 plateau, with the quantum-confined Stark effect leading to a significant tilt in the plateau as a function of gate voltage. Note that for the measurement results shown here the sample was characterized in a flow cryostat leading to higher temperature, i.e. higher resistivity, and therefore to a higher voltage range than in part (b).

spontaneous light emission. Part of this electroluminescence signal was recorded on our bottom detector when recording the *I*–*V* characteristics and is plotted in the same figure 3(b) (blue circles).

Recently, experiments based on photonic-crystal and micropillar technology demonstrated charge control of QD excitons [32–34], also in combination with resonant spectroscopy [35]. While all these approaches require rather sophisticated fabrication procedures, it turns out that the simple processing steps listed above are sufficient to obtain charge control in our fiber–cavity setting. Charge control is demonstrated in figure 3(d): here, PL emission was recorded as a function of the applied electric field. By means of their characteristic energy difference and voltage dependence, different charging states can be clearly identified in the spectrum, with the emission lines originating from the neutral exciton (X^0), biexciton (XX^0) and the positively (X^+) and negatively (X^-) charged excitons (trions) indicated in the plot. In addition, emission

involving other multiply charged states is visible. The capability to deterministically charge the QD allows us to selectively address trionic QD states and therefore make use of the spin degrees of freedom. The spin properties of the present sample were investigated (without a fiber mirror), and complete spin pumping in Faraday geometry [36] was found. The inset of figure 3(d) displays the energy shift of the neutral exciton line X^0 due to the quantum confined Stark effect as a function of the applied electric field. The significant Stark shift opens up the possibility of electrically tuning excitonic states into resonance with the cavity mode as will be demonstrated later in the paper.

6. Photoluminescence spectroscopy

To demonstrate coupling of the cavity mode to single QD transitions, we perform PL spectroscopy with an above-bandgap pulsed laser at 785 nm. The emitted photons from the coupled QD–cavity system are analyzed on a grating spectrometer. In a first experiment, we fix the QD gate voltage such that the X^0 exciton is stable. We continuously collect PL spectra while tuning the cavity length and thereby scanning the cavity resonance across the X^0 transition. The result of this measurement is shown in figure 4(a). The cavity resonance is detectable for all cavity lengths within the scanning range even at very low powers due to off-resonant cavity feeding [37, 38]. When the cavity resonance wavelengths for the two non-degenerate orthogonally linearly polarized modes TEM_{00}^A and TEM_{00}^B match the X^0 emission wavelengths around 977.3 nm, there is a clear increase in the detected intensity. A careful analysis, shown in figure 4(c), indicates that the detected intensity follows a Lorentzian line shape as a function of cavity length, which is to be expected for an emitter weakly coupled to a cavity.

As figure 4(b) illustrates, for other QD exciton emission lines, the wavelength at which the maximum intensity is detected differs for the TEM_{00}^A and TEM_{00}^B modes. We attribute this difference to the X–Y splitting [39] of the transitions of the X^0 charge state. For a single QD, the coupling strength of a particular transition to a given cavity mode depends on the relative angle between the QD axis and the direction of linear polarization of the mode. Thus, a rotator in the system would allow maximizing of the QD–cavity coupling by aligning the QD dipole emission along the cavity polarization axis.

A complementary PL spectrum can be obtained by fixing the cavity length and tuning the QD bias voltage, which in turn tunes the QD transition wavelengths via the quantum confined Stark effect. Such a spectrum is shown in figure 4(d). In this case, two spectrally close excitonic emissions, which we tentatively attribute to X^- and X^{2-}, are tuned in resonance with one of the cavity modes. Again, the detected intensity increases by an order of magnitude when the QD transitions are tuned to the cavity resonances.

We also made PL saturation measurements (pulsed excitation) with fixed cavity length and bias voltage, with the cavity wavelength tuned to a single QD excitonic transition. The intensity of the emitted light from the QD–cavity system as a function of excitation power is displayed in the inset of figure 4(a). The clear saturation behavior above a certain excitation power provides evidence that one and only one QD is coupled to the cavity mode for the particular wavelength detected here.

A real door-opener for a multitude of future experiments with our new system is its flexibility, reversibility and speed of tuning by either changing the cavity length or controlling the gate voltage, in particular when compared to more established techniques in other systems, such as gas deposition or temperature tuning [27, 40]. Another advantage of the present system

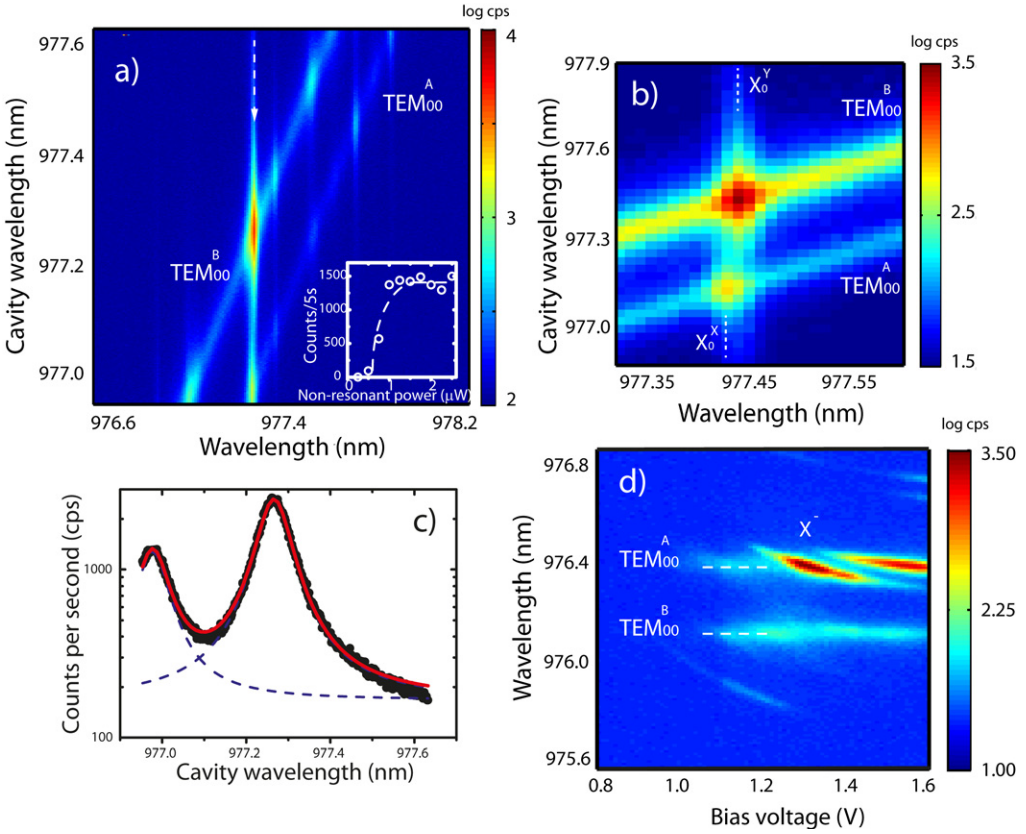

Figure 4. (a) Tuning the cavity resonance wavelength through single QD transitions. The data clearly show enhanced emission from the cavity–QD system when the cavity is resonant with single QD transitions (vertical PL lines). The inset shows the saturation behavior of the detected emission from the cavity–QD system as a function of off-resonant excitation power. (b) The two different polarization modes of the cavity (TEM_{00}^{A} and TEM_{00}^{B}) couple preferentially to one of the neutral exciton transitions. The coupling strength depends on the relative angle between the QD axis and cavity polarization. (c) Vertical cut of panel (a) showing PL as a function of cavity detuning (length). The data (black dots) are fitted by a Lorentzian (red line) showing the characteristics of a weak coupling of the QD to the cavity mode. (d) Voltage tuning of single QD lines to cavity modes. Here, we change the bias voltage in order to tune QD transitions via the quantum-confined Stark effect into resonance with the fundamental modes of the cavity. On resonance, the QD emission is clearly enhanced.

lies in the built-in fiber coupling, which allows for straightforward efficient probing using more sophisticated techniques such as high-resolution resonant spectroscopy.

7. Resonant spectroscopy

We performed resonant laser spectroscopy by measuring the transmission of a tunable diode laser through the coupled QD–cavity system using the transmission detector. Since the top fiber

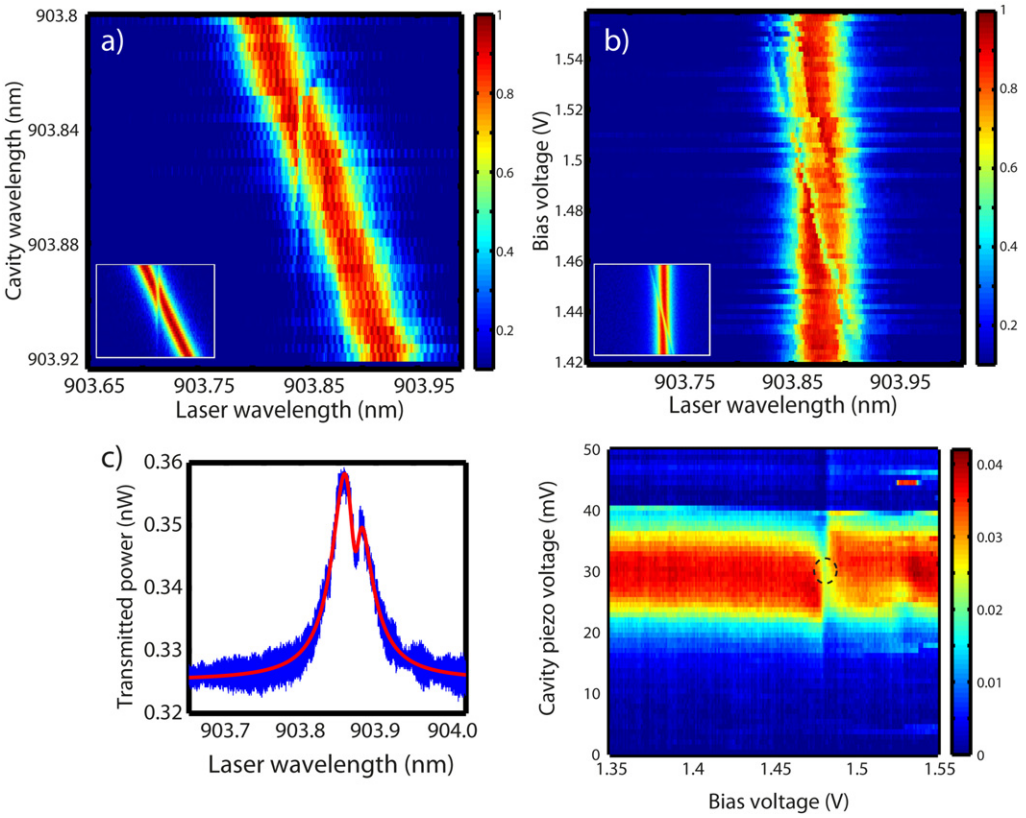

Figure 5. (a), (b) Two-dimensional (2D) color plots of the system transmission normalized to maximal transmission while scanning the resonant laser (horizontal axis) as a function of (a) the cavity length and (b) gate voltage. In (a), the wavelength of the QD transition stays constant, whereas in (b), the cavity resonance frequency is fixed. In both cases, a dip due to the coupling of the QD to the cavity mode is clearly visible where one expects QD resonance in the spectra. The two insets display corresponding calculated transmission spectra based on the model, and parameters, used in the text. (c) Single transmission spectrum from (b) at a bias voltage of 1.458 V. The contrast of the transmission dip is about 22%. (d) Keeping the laser wavelength fixed the system can be brought into resonance by a clever choice of both the cavity length and the gate voltage. The sweet spot of maximum coupling is marked by a black circle.

mirror has a higher reflectivity than that grown on the sample, most of the intra-cavity photons escape through that bottom mirror onto the photodiode. The transmission signal can be directly detected with a low-noise amplifier without the need for a lock-in technique.

Figure 5(a) shows the transmission (normalized to the maximum transmission) spectra as a function of resonant laser wavelength (horizontal axis) and cavity length (vertical axis). The QD modifies the Lorentzian transmission of the unperturbed cavity (top and bottom of the scan) by introducing a dispersive response fixed at the QD resonance. As we performed all the experiments well below saturation, we are able to extract the coupling parameters directly from

a fit to the data using the equation [41]

$$T = T_0 \left| \frac{\kappa/2}{\omega - \omega_{\mathrm{cav}} + \mathrm{i}\kappa/2 - \frac{g^2}{\omega - \omega_{\mathrm{QD}} + \mathrm{i}\gamma/2}} \right|^2, \tag{8}$$

where ω_{cav} is the cavity angular frequency, ω_{QD} is the QD transition angular frequency and T_0 is the bare cavity transmission. From the experimental data, we extract $\hbar g = 11.7\,\mu$eV, $\hbar\gamma = 11.4\,\mu$eV and $\hbar\kappa = 78\,\mu$eV. The inset of figures 5(a) and (b) shows a calculated spectral map using these parameters and the above expression (8).

In figure 5(b), the cavity length is kept constant while the bias voltage tunes the QD resonance through the cavity resonance. Note that for each spectrum the background electroluminescence (figure 2(b)) seen by the transmission detector was subtracted and finally normalized to the peak transmission. Again as in figure 5(a), the QD significantly modifies the transmission spectrum through the cavity.

We plot equation (8) using previously extracted parameters in the inset of figure 5(b). Figure 5(c) shows a horizontal line cut taken from the data presented in figure 5(b) at a bias voltage of 1.458 V (blue line) and its corresponding fit (red line). The dip appearing in the transmission in figures 5(a)–(c) when the laser is on resonance with the exciton is a spectacular signature of the quantum interference effect [42].

The great flexibility of our system is best illustrated by the fact that one can demonstrate the QD–cavity coupling with an almost randomly chosen laser wavelength by adjusting the cavity length and QD bias voltage simultaneously. We demonstrate this by parking the laser at a wavelength of 903.865 nm and scanning both the cavity length and gate voltage. The resulting 2D map is displayed in figure 5(d). Vertical cuts show a sweep of the cavity length across the laser for a given QD–laser detuning. Horizontal cuts show gate voltage sweeps for a given cavity-laser detuning. A gate voltage sweep causes a shift in the QD emission (cf figure 3(d)). The gate voltage at which the QD is tuned to the laser is 1.482 V, as seen in the figure, with the full resonance condition (no detuning between laser, cavity and QD emission energies) indicated by a black circle.

8. The onset of unity cooperativity and strong coupling

A particulary interesting regime for experiments in cavity QED is the regime of strong coupling where the photon exchange between the emitter and cavity modes is as fast as or faster than the photon decay from the system. In this regime, new eigenstates, the so-called polaritons, form. In general, the eigenenergies of the coupled QD–cavity system can be determined from the equation [43]

$$\omega_{\pm} = \frac{\omega_{\mathrm{cav}} + \omega_{\mathrm{QD}}}{2} - \mathrm{i}\frac{\kappa + \gamma}{4} \pm \sqrt{g^2 - \left(\frac{\kappa - \gamma}{4} - \mathrm{i}\frac{\omega_{\mathrm{QD}} - \omega_{\mathrm{cav}}}{2}\right)^2}. \tag{9}$$

By carefully positioning the QD and the cavity relative to each other, the coupling strength can be optimized by reading out the PL counts. Once an optimally coupled QD was found, we recorded resonant transmission spectra as a function of cavity length as displayed in figure 6(a). Clearly, when crossing the QD resonance, the cavity mode splits into two distinct peaks which form an avoided level crossing. There is a telegraphic noise contribution to the overall noise in the measurements originating from the current flowing through the device.

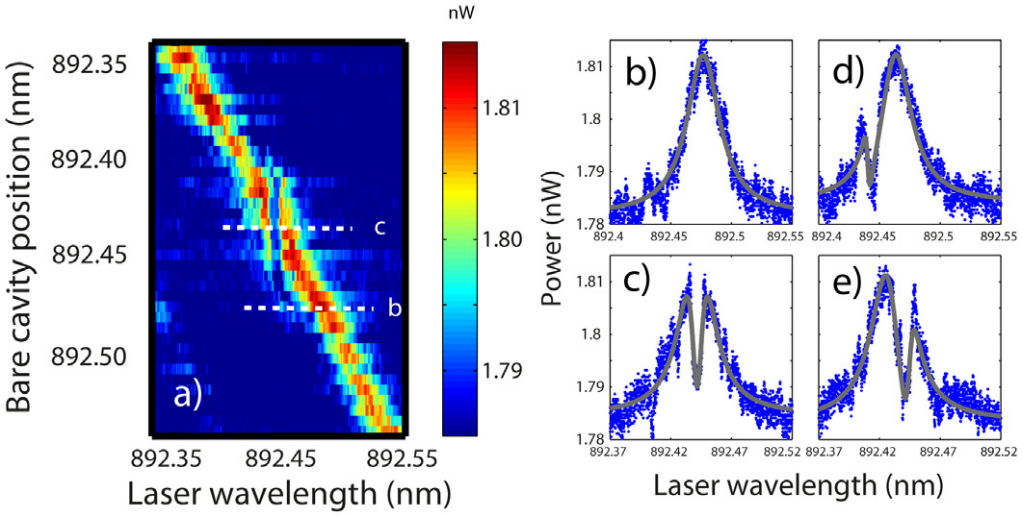

Figure 6. The onset of strong coupling: (a) transmission as a function of cavity length and laser frequency. Panels (b)–(e) display several cut offs from panel (a): blue dots represent the data and gray lines are fits to the data.

Fits to the data (see, e.g., figures 6(b) to (e)) yield $\hbar g = 12.3 \pm 2.5\,\mu$eV, $\hbar\kappa = 50.0 \pm 2.7\,\mu$eV and $\hbar\gamma = 3.1 \pm 0.7\,\mu$eV, which implies that for this particular QD with a narrow linewidth, the system is at the onset of strong coupling with $2g \approx (\kappa + \gamma)/2$ [44].

The present QD–cavity system has a cooperativity of $C \approx 2.0 \pm 1.3$. In order to enlarge this number significantly, different strategies can be adopted: increasing the number of layers of the DBR semiconductor stack while simultaneously reducing the doping density in the p- and n-layers should decrease κ significantly. In addition, a smaller radius of curvature of the fiber mirror (a radius of curvature as small as 20 μm has been reported [45]) would reduce the effective mode volume of the cavity and hence increase g. On the emitter side, other QD systems such as quantum-well monolayer fluctuations with oscillator strengths up to one order of magnitude larger [10] could push the system much deeper into the strong-coupling regime, thereby increasing the cooperativity up to an order of magnitude.

9. Conclusions and outlook

In this paper, we have presented a very versatile QD–microcavity platform for performing state-of-the-art cavity QED experiments. The system is fully tunable, i.e. both cavity length and QD energy can be controlled at will. The high Q of our system together with the moderate mode volume brings us into the high-cooperativity regime where the coherent interaction starts to dominate the system dynamics. The onset of strong coupling was demonstrated through the observation of an avoided level crossing in resonant transmission spectroscopy. We anticipate that with some simple improvements on both the cavity and emitter sides, the system can enter deeply into the strong-coupling regime. The ability to control the charge state of the QD by means of the p–i–n structure will allow us to perform experiments on quantum information processing, with a first step being the demonstration of an efficient fiber-coupled spin–photon interface [46]. Our QD–fiber–cavity system might then serve as a node in a future

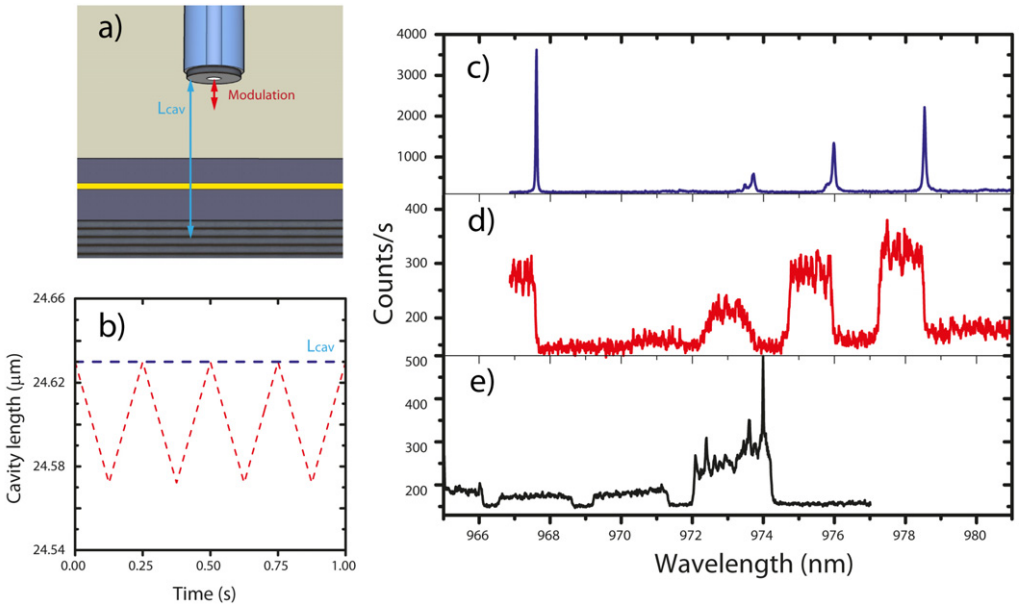

Figure A.1. The principle of the modulated cavity is shown in panel (a): for a given cavity length, we impose a triangle modulation (b) to create broader spectral windows through the cavity modes. Panel (c) shows the PL spectrum for a cavity length of $\approx$43 μm integrated over 1 s. The same spectrum broadened by the modulation (4 Hz, $\approx$58 nm amplitude) is shown in (d). Panel (e) shows the spectrum for a shorter cavity ($\approx$24.6 μm) and the same modulation (5 s integration time) when the cavity mode is spatially and spectrally aligned to a QD: the QD lines over the TEM_{00} are clearly visible.

solid-state-based quantum network [47, 48] similarly to what has been demonstrated with atom–cavity interfaces [49].

Acknowledgments

We thank F Kaeding, S Smolka and W Wuester for help in processing the samples, M Kroner for helpful discussions and the ohmic annealing oven, W Gao and P Fallahi for helpful discussions and the spin pumping measurements and the ETHZ D-PHYS workshop for the fabrication of the dip stick. We acknowledge support through NCCR quantum photonics, an instrument of the Swiss National Science Foundation, and through the SOLID project ('Solid state systems for quantum information processing') from the Quantum Information Processing and Communication in Europe program.

Appendix. Cavity modulation for QD spectroscopy

The sample is not always perfectly mounted flat owing to fixing imperfections, and it can have a slight angle with respect to the fiber. Hence, when performing horizontal scans with the fiber cavity, the resonance of the cavity changes with horizontal position (for a fixed vertical piezo position) due to the change in length of the cavity. This makes some of the experiments requiring

horizontal scanning (determination of the mode profiles for example) more involved, since the resonance of the cavity easily shifts away from QD resonance. Here, we overcome this difficulty by modulating the cavity length, $L_{\mathrm{eff}}(t) = L^0_{\mathrm{eff}} + f(t)$, with a triangular waveform at a frequency ω_{osc}. The amplitude $f(t)$ thereby varies between f_{max} and f_{min}. This way, small perturbations in cavity length do not matter anymore, provided the optical signal is acquired with a time constant $t \gg 2\pi/\omega_{\mathrm{osc}}$. On the spectrometer, the narrow cavity modes are transformed into broad rectangular resonances with a width given by

$$\Delta\nu_{\mathrm{window}} = (c/2n_{\mathrm{eff}})(1/(L^0_{\mathrm{eff}} + f_{\mathrm{min}}) - 1/(L^0_{\mathrm{eff}} + f_{\mathrm{max}})). \tag{A.1}$$

An example of such a spectrum is shown in figure A.1(c). There we can see the PL of a spectrum of the static cavity. As schematically shown in figures A.1(a) and (b), by applying a zigzag (triangular) modulation of a frequency of 4 Hz and an amplitude of only ≈58 nm, we obtain the spectra seen in figure A.1(d). There we can observe the broad window through which we can detect the luminescence. As seen in figure 3(b) still by scanning horizontally the cavity the central frequency of the cavity will shift with position (dashed lines in figure 3(b)), but any QD measured within the modulated cavity window can be analyzed (QD1 in figure 3(b). An example spectrum of QDs through the TEM_{00} is shown in figure A.1(e). Additionally, from the slope of the dashed lines in figure 3(b) we could extract the sample–fiber tip tilt of 0.15°.

References

[1] Purcell E M 1946 Spontaneous emission probabilities at radio frequencies *Phys. Rev.* **69** 681

[2] Birnbaum K M, Boca A, Miller R, Boozer A D, Northup T E and Kimble H J 2005 Photon blockade in an optical cavity with one trapped atom *Nature* **436** 87–90

[3] Tanji-Suzuki H, Chen W, Landig R, Simon J and Vuletić V 2011 Vacuum-induced transparency *Science* **333** 1266–9

[4] Lugiato L A 1984 *Progress in Optics* vol 21 (Amsterdam: Elsevier)

[5] Koch M, Sames C, Balbach M, Chibani H, Kubanek A, Murr K, Wilk T and Rempe G 2011 Three-photon correlations in a strongly driven atom–cavity system *Phys. Rev. Lett.* **107** 023601

[6] Dayan B, Parkins A S, Aoki T, Ostby E P, Vahala K J and Kimble H J 2008 A photon turnstile dynamically regulated by one atom *Science* **319** 1062–5

[7] Wallraff A, Schuster D I, Blais A and Frunzio L 2004 Strong coupling of a single photon to a superconducting qubit using circuit quantum electrodynamics *Nature* **431** 162

[8] Reithmaier G S J P, Löffler A, Hofmann C, Kuhn S, Reitzenstein S, Keldysh L V, Kulakovskii V D and Reinecke A F T L 2004 Strong coupling in a single quantum dot–semiconductor microcavity system *Nature* **432** 197–200

[9] Yoshie T, Scherer A, Hendrickson J, Khitrova G, Gibbs H M, Rupper G, Ell C, Shchekin O B and Deppe D G 2004 Vacuum Rabi splitting with a single quantum dot in a photonic crystal nanocavity *Nature* **432** 200–3

[10] Peter E, Senellart P, Martrou D, Lemaître A, Hours J, Gérard J M and Bloch J 2005 Exciton–photon strong-coupling regime for a single quantum dot embedded in a microcavity *Phys. Rev. Lett.* **95** 67401

[11] Hennessy K, Badolato A, Petroff P M and Hu E 2004 Positioning photonic crystal cavities to single InAs quantum dots *Photon. Nanostruct.—Fundam. Appl.* **2** 65–72

[12] Mohan A, Felici M, Gallo P, Dwir B, Rudra A, Faist J and Kapon E 2010 Polarization-entangled photons produced with high-symmetry site-controlled quantum dots *Nature Photon.* **4** 302–6

[13] Dousse A, Lanco L, Suffczyński J, Semenova E, Miard A, Lemaître A, Sagnes I, Roblin C, Bloch J and Senellart P 2008 Controlled light–matter coupling for a single quantum dot embedded in a pillar microcavity using far-field optical lithography *Phys. Rev. Lett.* **101** 267404

[14] Cui G *et al* 2006 A hemispherical, high-solid-angle optical micro-cavity for cavity-QED studies arXiv:quant-ph/0601046
[15] Muller A, Flagg E B, Metcalfe M, Lawall J and Solomon G S 2009 Coupling an epitaxial quantum dot to a fiber-based external-mirror microcavity *Appl. Phys. Lett.* **95** 173101
[16] Barbour R J, Dalgarno P A, Curran A, Nowak K M, Baker H J, Hall D R, Stoltz N G, Petroff P M and Warburton R J 2011 A tunable microcavity *J. Appl. Phys.* **110** 053107
[17] Jaynes E T and Cummings F W 1963 Comparison of quantum and semiclassical radiation theories with application to the beam maser *Proc. IEEE* **51** 89–109
[18] Andreani L C, Panzarini G and Gérard J M 1999 Strong-coupling regime for quantum boxes in pillar microcavities: theory *Phys. Rev.* B **60** 13276
[19] Englund D, Faraon A, Fushman I, Stoltz N and Pierre Petroff J V 2007 Controlling cavity reflectivity with a single quantum dot *Nature* **450** 857–61
[20] Srinivasan K and Painter O 2007 Linear and nonlinear optical spectroscopy of a strongly coupled microdisk–quantum dot system *Nature* **450** 862–5
[21] Schneider C, Huggenberger A, Gschrey M, Gold P, Rodt S, Forchel A, Reitzenstein S, Höfling S and Kamp M 2012 In(Ga) as-GaAs site-controlled quantum dots with tailored morphology and high optical quality *Physica Status Solidi* a **209** 2379–86
[22] Jöns K D, Atkinson P, Müller M, Heldmaier M, Ulrich S M, Schmidt O G and Michler P 2013 Triggered indistinguishable single-photons with narrow linewidths from site-controlled quantum dots *Nano Lett.* **13** 126
[23] Badolato A, Hennessy K, Atatüre M, Dreiser J, Hu E, Petroff P M and Imamoğlu A 2005 Deterministic coupling of single quantum dots to single nanocavity modes *Science* **308** 1158–61
[24] Thon S M, Rakher M T, Kim H, Gudat J, Irvine W, Petroff P M and Bouwmeester D 2009 Strong coupling through optical positioning of a quantum dot in a photonic crystal cavity *Appl. Phys. Lett.* **94** 111115
[25] Dousse A, Suffczynski J, Braive R, Miard A, Lemaître A, Sagnes I, Lanco L, Bloch J, Voisin P and Senellart P 2009 Scalable implementation of strongly coupled cavity–quantum dot devices *Appl. Phys. Lett.* **94** 121102
[26] Hennessy K, Badolato A, Tamboli A, Petroff P M, Hu E, Atature M, Dreiser J and Imamoglu A 2005 Tuning photonic crystal nanocavity modes by wet chemical digital etching *Appl. Phys. Lett.* **87** 021108
[27] Mosor S, Hendrickson J, Richards B C, Sweet J, Khitrova G, Gibbs H M, Yoshie T, Scherer A, Shchekin O B and Deppe D G 2005 Scanning a photonic crystal slab nanocavity by condensation of xenon *Appl. Phys. Lett.* **87** 141105
[28] Hunger D, Steinmetz T, Colombe Y, Deutsch C, Hänsch T W and Reichel J 2010 A fiber Fabry–Perot cavity with high finesse *New J. Phys.* **12** 065038
[29] Panzarini G, Andreani L C, Armitage A, Baxter D, Skolnick M S, Astratov V N, Roberts J S, Kavokin A V, Vladimirova M R and Kaliteevski M A 1999 Exciton–light coupling in single and coupled semiconductor microcavities: polariton dispersion and polarization splitting *Phys. Rev.* B **59** 5082
[30] Savona V 1999 Linear optical properties of semiconductor microcavities with embedded quantum wells *Confined Photon Systems: Fundamentals and Applications* (*Lecture Notes in Physics* vol 531) ed H Benisty, J-M Gérard, R Houdré, J Rarity and C Weisbuch (Berlin: Springer) pp 173–242
[31] Garcia J *et al* 1997 Intermixing and shape changes during the formation of InAs self-assembled quantum dots *Appl. Phys. Lett.* **71** 2014–6
[32] Laucht A, Hofbauer F, Hauke N, Angele J, Stobbe S, Kaniber M, Böhm G, Lodahl P, Amann M C and Finley J J 2009 Electrical control of spontaneous emission and strong coupling for a single quantum dot *New J. Phys.* **11** 023034
[33] Rakher M T, Stoltz N G, Coldren L A, Petroff P M and Bouwmeester D 2009 Externally mode-matched cavity quantum electrodynamics with charge-tunable quantum dots *Phys. Rev. Lett.* **102** 97403
[34] Reitzenstein S *et al* 2011 Electrically driven quantum dot micropillar light sources *IEEE J. Sel. Top. Quantum Electron.* **17** 1670–80
[35] Pinotsi D, Fallahi P, Miguel-Sanchez J and Imamoglu A 2011 Resonant spectroscopy on charge tunable quantum dots in photonic crystal structures *IEEE J. Quantum Electron.* **47** 1371–4

[36] Atature M, Dreiser J, Badolato A, Hogele A, Karrai K and Imamoglu A 2006 Quantum-dot spin-state preparation with near-unity fidelity *Science* **312** 551–3
[37] Winger M *et al* 2009 Explanation of photon correlations in the far-off-resonance optical emission from a quantum-dot–cavity system *Phys. Rev. Lett.* **103** 207403
[38] Yamaguchi M, Asano T and Noda S 2012 Third emission mechanism in solid-state nanocavity quantum electrodynamics *Rep. Prog. Phys.* **75** 096401
[39] Gammon D, Snow E S, Shanabrook B V, Katzer D S and Park D 1996 Fine structure splitting in the optical spectra of single GaAs quantum dots *Phys. Rev. Lett.* **76** 3005–8
[40] Winger M, Badolato A, Hennessy K J, Hu E L and Imamoğlu A 2008 Quantum dot spectroscopy using cavity quantum electrodynamics *Phys. Rev. Lett.* **101** 226808
[41] Auffèves-Garnier A, Simon C, Gérard J-M and Poizat J-P 2007 Giant optical nonlinearity induced by a single two-level system interacting with a cavity in the Purcell regime *Phys. Rev.* A **75** 053823
[42] Tanji-Suzuki H, Leroux I D, Schleier-Smith M H, Cetina M, Grier A T, Simon J and Vuletić V 2011 *Advances in Atomic, Molecular and Optical Physics* (vol 60) (Amsterdam: Elsevier)
[43] Reitzenstein S 2012 Semiconductor quantum dot–microcavities for quantum optics in solid state *IEEE J. Sel. Top. Quantum Electron.* **18** 1733–46
[44] Khitrova G, Gibbs H M, Kira M, Koch S W and Scherer A 2006 Vacuum Rabi splitting in semiconductors *Nature Phys.* **2** 81–90
[45] Hunger D, Deutsch C, Barbour R J, Warburton R J and Reichel J 2012 Laser micro-fabrication of concave, low-roughness features in silica *AIP Adv.* **2** 012119
[46] Yılmaz S T, Fallahi P and Imamoğlu A 2010 Quantum-dot-spin single-photon interface *Phys. Rev. Lett.* **105** 33601
[47] Gao W B, Fallahi P, Togan E, Miguel-Sanchez J and Imamoglu A 2012 Observation of entanglement between a quantum dot spin and a single photon *Nature* **491** 426–30
[48] De Greve K *et al* 2012 Quantum-dot spin-photon entanglement via frequency downconversion to telecom wavelength *Nature* **491** 421–5
[49] Ritter S, Nolleke C, Hahn C, Reiserer A, Neuzner A, Uphoff M, Mucke M, Bochmann J and Rempe G 2012 An elementary quantum network of single atoms in optical cavities *Nature* **484** 195–200